Influence of the support on Ni catalysts performance in the in-line steam reforming of biomass fast pyrolysis derived volatiles

Laura Santamaria, Gartzen Lopez[*], Aitor Arregi, Maider Amutio, Maite Artetxe, Javier Bilbao, Martin Olazar

Department of Chemical Engineering, University of the Basque Country UPV/EHU, P.O. Box 644, E48080 Bilbao, Spain

ABSTRACT

The influence the support has on the performance of Ni catalysts used in the reforming of biomass fast pyrolysis volatiles has been assessed. Accordingly, five catalysts have been prepared by wet impregnation method, namely Ni/Al_2O_3, Ni/SiO_2, Ni/MgO, Ni/TiO_2 and Ni/ZrO_2. These catalysts have been characterized by nitrogen adsorption/desorption, X-ray fluorescence spectroscopy, temperature programmed reduction and X-ray diffraction techniques. The pyrolysis-reforming runs have been performed in a bench scale unit operating in continuous regime. The biomass (pine wood sawdust) pyrolysis step has been carried out in a conical spouted bed reactor at 500 °C, with the volatiles produced (a mixture of gases and bio-oil) being reformed in-line on the prepared catalysts in a fluidized bed reactor at 600 °C. Remarkable differences have been observed amongst the catalyst prepared, with Ni/Al_2O_3, Ni/MgO and Ni/ZrO_2 being those leading to the most encouraging results, whereas Ni/TiO_2 and, especially Ni/SiO_2, having a limited reforming activity. The performance of each catalyst has been related to its properties determined in the characterization.

1. Introduction

The environment problems associated with the dependence on fossil fuels have increased the interest of biomass as renewable source in order to contribute to reducing CO_2 emissions [1]. Thus, thermochemical processes for biomass valorisation, particularly gasification and fast pyrolysis, are of special interest, as they can be implemented in full scale units and their products, syngas and bio-oil, respectively, are promising intermediate products that can be further converted into commercial fuels and chemicals [2,3].

Hydrogen production is a preferential objective in the valorisation of biomass due to the growing demand of H_2 as energy carrier, fuel and raw material, given that around 96% of H_2 is currently produced from fossil fuels [4]. Thus, biomass steam gasification allows producing H_2 rich syngas [5,6]. However, the implementation of this process is limited by the high tar content in the syngas [7]. Steam reforming of bio-oil (product of biomass fast pyrolysis) is an interesting indirect route for H_2 production from biomass due to the high H_2 selectivity and full conversion of the tars attained [8–14]. Bio-oil is a very complex mixture of oxygenated compounds of different nature [15,16].

As an alternative to H_2 production from bio-oil, pyrolysis and in-line reforming of the volatiles has also been proposed as a direct strategy for H_2 production from biomass [17–22] and other residues, such as waste

plastics [23–26]. Interestingly, H_2 production can be considerably increased by co-feeding plastics with biomass in the pyrolysis-reforming process [27,28]. Moreover, the direct alternative of pyrolysis and in-line reforming avoids the handling of bio-oil, specially the problems associated with its storage and vaporization [13,29]. In fact, this process involves several operational advantages, as are: (i) separate optimization of pyrolysis and reforming conditions, (ii) lower temperature than gasification, which reduces material costs and catalyst sintering problems, (iii) avoids the direct contact of the catalyst with the impurities contained in the biomass (they are retained in the pyrolysis reactor).

However, both direct and indirect routes for the reforming of biomass derived products are conditioned by the fast catalyst deactivation due to coke formation. Thus, the unstable nature of bio-oil oxygenates undergo decomposition reactions that lead to severe coke formation on the reforming catalyst [11,29,30]. Amongst the catalysts studied in the literature, most of them are Ni based ones because this metal combines a suitable activity (significant capacity for C−C, C−H and O−H bond cleavage) [31] with a considerably lower price than other noble metals [32,33]. Nevertheless, Ni is less active for water gas shift (WGS) reaction and promotes methanation and coke formation reactions [34].

Several strategies have been proposed in order to improve Ni catalysts performance, with the most common ones being based on the

selection of the right support and subsequent modifications [9,35]. In fact, the support plays a key role on catalyst performance, as it stabilizes the metal and may also take part in secondary reactions, thereby controlling coke deposition [11]. Therefore, a suitable oxide should provide a strong metal-support interaction, which enhances Ni dispersion and minimizes metal sintering [36]. Furthermore, it should promote oxygen mobility and have high oxygen storage capacity in order to ease the removal of carbonaceous deposits and attenuate deactivation [35]. A wide range of Ni supported catalyst have been proposed in the literature for the reforming of bio-oil, bio-oil model compounds and biomass pyrolysis volatiles, with Al_2O_3 [22,37–39], ZrO_2 [38,40], MgO [20,38,41], CeO_2 [38,40] and dolomite [42–44] being extensively used.

Although great effort has been devoted to the development of catalysts for the reforming of bio-oil model compounds, the studies conducted by feeding crude bio-oil are scarce [9]. Therefore, knowledge of the performance of reforming catalysts under real process conditions is still limited. Accordingly, this study analyzes the influence the support in Ni catalysts has on the reforming of the whole biomass pyrolysis volatile stream, i.e. the gases and bio-oil produced. Thus, catalyst screening was carried out based on a bench scale pyrolysis-reforming unit operating in continuous regime. The pyrolysis step was performed in a conical spouted bed reactor (CSBR), whose features allow operating under flash pyrolysis conditions and enhance bio-oil yield [45,46]. The subsequent step of catalytic steam reforming of pyrolysis volatiles was conducted in a fluidized bed reactor (FBR). This original pyrolysis-reforming process has already been applied to the valorisation of biomass [19], different plastics [24,25] and biomass/plastics mixtures [27] on a commercial Ni catalyst in the reforming step.

2. Materials and methods

2.1. Materials

The biomass used in this study was pine wood (Pinus insignis), which was crushed and sieved to a particle size between 1 and 2 mm. It was then dried at room temperature to a moisture content below 10 wt %. The main properties of the pine wood sawdust are set out in Table 1. The ultimate and proximate analyses have been determined in a LECO CHNS-932 elemental analyzer and in a TGA Q5000IR thermogravimetric analyzer, respectively. The higher heating value (HHV) has been measured in a Parr 1356 isoperibolic bomb calorimeter. The thermal degradation behaviour of this biomass has been reported elsewhere [47].

2.2. Catalyst synthesis

Several supported nickel catalysts were prepared by wet impregnation of the support with an aqueous solution of $Ni(NO_3)_2 \cdot 6H_2O$ *(VWR Chemicals, 99%)*. The commercial metal oxides used as catalyst supports were γ-Al_2O_3 *(Alfa Aesar)*, SiO_2 *(Merck)*, MgO *(Sigma Aldrich)*, TiO_2 *(Alfa Aesar)* and ZrO_2 *(Alfa Aesar)*.

Prior to loading Ni, the Al_2O_3 was pretreated by calcination under

Table 1
Biomass characterization (Pine wood).

Ultimate analysis (wt%)	
Carbon	49.33
Hydrogen	6.06
Nitrogen	0.04
Oxygen	44.57
Proximate analysis (wt%)	
Volatile matter	73.4
Fixed carbon	16.7
Ash	0.5
Moisture	9.4
HHV (MJ kg^{-1})	19.8

air atmosphere at 1000 °C for 5 h to thermally stabilize the support, thus avoiding any possible phase change of γ-Al_2O_3 during the process, as well as improving the mechanical strength of the catalyst. All supports were adequately ground and sieved to a particle size between 0.4 and 0.8 mm, given that this particle size was determined as the most suitable one for use in fluidized bed reforming reactors [19]. Ni wet impregnation was carried out under vacuum at 70 °C (Büchi rotavapor R-114) using 10 ml of solution per g of support in all the catalysts prepared.

After impregnation, the catalysts were dried at 100 °C overnight and subsequently calcined at 700 °C for 3 h, except the Ni/MgO one, which was calcined at 500 °C. Based on previous studies on the optimum Ni loading [48], Ni content was fixed at 10 wt% because higher loads led to severe deactivation by sintering [49].

2.3. Catalyst characterization

The physical properties of the catalyst (specific surface area, pore volume and average pore size) have been determined by N_2 adsorption–desorption isotherms at 77K in a Micromeritics ASAP 2010. Surface area was calculated based on the BET equation, whereas the pore size distribution was determined by BJH method. Prior to the analyses the samples were outgassed under vacuum at 150 °C for 8 h.

X-ray fluorescence (XRF) spectrometry was used to measure the total metal loading (wt%) of each catalyst. From each powder sample, a borated glass bead was prepared by melting it in an induction microfurnace. The flux Spectromelt A12 from Merck and the samples were mixed in a ratio of approximately 20:1.

The chemical analysis of the beads was carried out under vacuum atmosphere using a sequential wavelength dispersion X-ray fluorescence (WDXRF) spectrometer (Axios 2005, PANalytical) equipped with a Rh tube, and three detectors (gaseous flow, scintillation and Xe sealing). The calibration lines were performed by means of well characterized international patterns of rocks and minerals.

Temperature Programmed Reduction (TPR) measurements were carried out to determine the reduction temperature of the different metallic phases in the catalyst. These assays were conducted in an AutoChem II 2920 Micromeritics. Prior to the reduction experiments, the catalysts were thermally treated under helium stream at 200 °C in order to remove water or any impurities. TPR profiles were recorded from room temperature to 900 °C under a flow of 10% H_2/Ar at a heating rate of 5 °C/min.

X-ray powder diffraction (XRD) patterns were recorded on a Bruker D8 Advance diffractometer with $CuK_{\alpha 1}$ radiation in order to analyse the crystalline structure of the calcined and reduced supports. The average Ni crystallite size was calculated by using the Scherrer formula. Moreover, Ni dispersion was determined based on the average Ni particle size and crystallite size, and this method provided similar results to the one based on H_2 adsorption [21,50]. However, certain differences were reported for Ni/TiO_2 due to the strong metal-support interaction [38]. The device is equipped with a Germanium primary monochromator, Bragg-Brentano geometry, with a $CuK_{\alpha 1}$ wavelength of 1.5406 (Å), corresponding to an X-ray tube with Cu anticathode. Sol-X dispersive energy detector was employed, with a window optimized for $CuK_{\alpha 1}$ for limiting the fluorescence radiation. Data collection was carried out continuously, from 10° to 80° with steps of 0.04° in 2θ and a measurement time per step of 12 s.

2.4. Equipment and reactors

The experiments were performed in a bench scale plant operating in continuous regime, whose scheme is shown in Fig. 1. The plant is made up of two reactors connected in line, i.e., biomass pyrolysis was carried out in a conical spouted bed reactor (CSBR) and the pyrolysis volatiles formed (gases + bio-oil) were transferred to a fluidised bed reactor (FBR) for the reforming step.
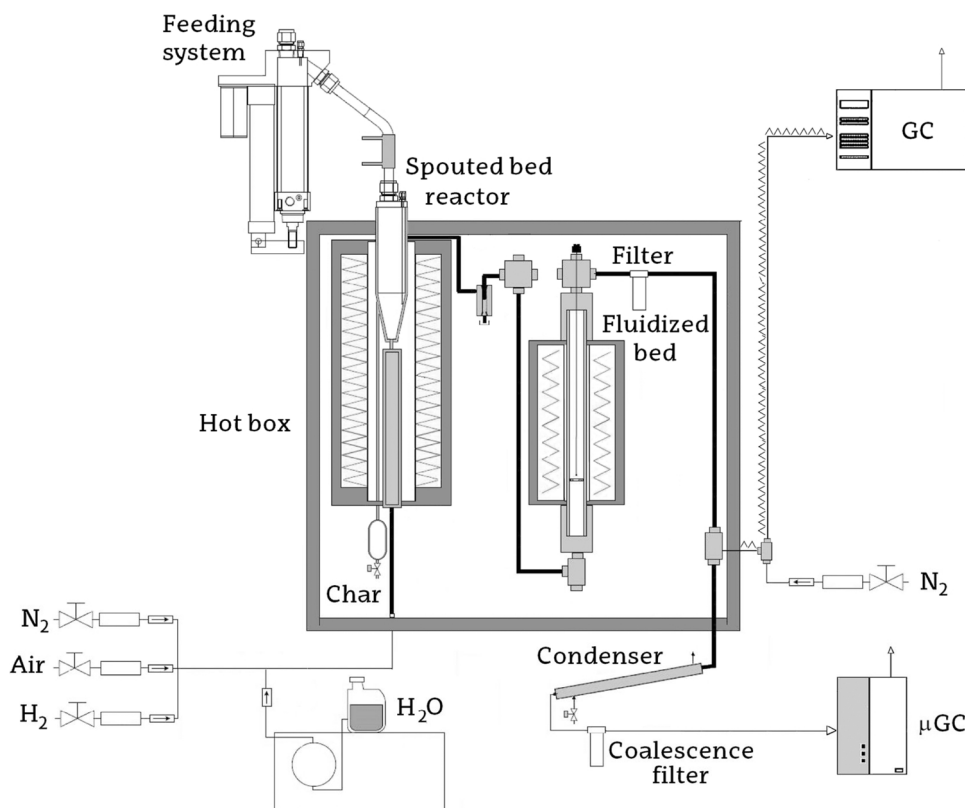
Fig. 1. Bench scale plant for continuous pyrolysis-reforming of biomass.

The CSBR has proven to perform well in previous pyrolysis studies in which several wastes were used, such as biomass [45,46,51], plastics [52,53] and tyres [54,55]. The dimensions of the pyrolysis reactor guarantee a stable spouting regime characterized by high heat and mass transfer rates and short residence times of the volatiles. Biomass pyrolysis was therefore performed under fast conditions. These dimensions are as follows: height of the conical section, 73 mm; diameter of the cylindrical section, 60.3 mm; angle of the conical section, 30°; diameter of the bed bottom, 12.5 mm, and diameter of the gas inlet, 7.6 mm. In addition, the reactor has a lateral outlet pipe placed above the bed surface for the removal of char particles from the bed (Fig. 1), thus minimising secondary reactions of pyrolysis volatiles. Below the reactor there is a gas preheater filled with stainless steel pipes in order to improve heat transfer. A 1250 W radiant oven heated the pyrolysis reactor, with temperature being controlled by two K-type thermocouples located inside the reactor, one in the bed annular region and the other one close to the reactor wall.

The volatile products of the pyrolysis step (gases and bio-oil) were reformed in line in a FBR. This reactor guarantees bed isothermicity and minimizes operational problems that are usual in fixed bed reactors, such as bed clogging due to severe coke formation [41,56–58]. In addition, a FBR is a suitable alternative for scaling up the process, as it allows the implementation of catalyst circulation strategies. The diameter of this reactor was 38.1 mm and its length 440 mm. The reactor was located in a radiant oven (550 W) and temperature was controlled by means of a thermocouple placed in the catalyst bed.

In order to avoid the condensation of steam and biomass pyrolysis products, the reaction zone (the pyrolysis and reforming reactors), the interconnection pipes, the cyclone and the filter were located inside a forced convection oven kept at 270 °C. The cyclone retains the fine char particles entrained from the pyrolysis step, and therefore avoids their feed into the reforming reactor, whereas the filter (5 μm sintered steel) retains the reforming catalyst fines elutriated from the reforming reactor.

Biomass was continuously fed into the pyrolysis reactor driven by an automatic feeder, which consists of a vessel equipped with a vertical shaft connected to a piston placed below the biomass bed. By raising the piston at the same time as the whole system was vibrated by an electric engine, the feeding system discharges the biomass through a pipe to the reactor. This pipe was cooled with tap water to avoid biomass partial degradation, and therefore system blockage. Moreover, a very small nitrogen flow rate introduced into the vessel stops the steam entering the feeding vessel.

The water flow rate was measured up by means of a high precision Gilson 307 pump. Once the water reached the forced convection oven, it was vaporized by means of an electric heater, and the steam was fed into the pyrolysis reactor. The plant has three mass flow meters for N_2, air and H_2, with N_2 being only used as fluidizing agent during the heating process prior to the reaction, and H_2 to reduce the Ni catalyst prior to the reforming reaction.

Non-reacted steam and bio-oil were retained in the condensation system prior to the gas analysis section. The volatile condensation system consists of a condenser (cooled with tap water) and a coalescence filter.

2.5. Experimental conditions

The hydrodynamic conditions in the CSBR and FBR were fine tuned in previous studies [19,24]. This point is critical given that the same steam flow acts as fluidizing agent in both reactors. In order to meet satisfactory fluidization regimes in both reactors, solid particle sizes were carefully selected. Thus, the CSBR contains 30 g of silica sand with a particle size in the 0.3–0.35 mm range. In the case of the FBR, the bed was made up of a mixture of reforming catalyst and inert sand, with the total bed mass being kept constant at 25 g in all the runs. The catalyst/sand mass ratios used were chosen according to the space time studied. The particle size of the catalyst was in the 0.4–0.8 mm range and that of the inert sand in the 0.3–0.35 mm range.

In all the experiments performed, the pyrolysis step temperature was fixed at 500 °C, which is the one determined as optimum for the pyrolysis of this material in a CSBR [45]. Likewise, reforming temperature was kept at 600 °C in all the experiments, given that similar results were obtained in a previous study conducted in the 600–700 °C range [19]. Furthermore, Ni sintering is avoided operating at 600 °C, as this temperature is slightly above pure Ni Tamman temperature [59]. Prior to the reforming reaction, the catalyst has been subject to an in situ reduction process at 710 °C for 4 h under a 10% vol. H$_2$ stream.

A steam/biomass (S/B) ratio of 4 was used in all the experiments, with continuous biomass feed rate being 0.75 g min^{-1} and that of the steam 3 g min^{-1}. Thus, the molar steam/carbon (S/C) ratio in the reforming step was 7.7. It should be noted that the amount of carbon contained in the char formed in the pyrolysis step was not considered in the calculation of this ratio. Two different space time values (10 and 20 g$_{cat}$ min g$_{volatiles}$$^{-1}$) were assayed for all the catalysts studied.

The experiments were carried out in continuous regime, and the GC and micro GC analyses were performed subsequent to several minutes of operation in order to ensure steady state conditions. Moreover, the runs have been repeated at least 3 times under the same conditions in order to guarantee reproducibility of the results.

2.6. Product analysis

Samples of the volatile stream leaving the reforming reactor were analysed on-line by means of a GC Varian 3900 provided with a HP-Pona column and a flame ionization detector (FID). It should be noted that FID detector response is not proportional to mass in the case of oxygenates. Accordingly, response factors have been used in order to ensure an accurate quantification of bio-oil compounds. The response factors used were based on those determined in previous studies dealing with bio-oil characterization [60]. The sample was injected into the GC by means of a line thermostated at 280 °C, once the reforming reactor outlet stream has been diluted with an inert gas in order to avoid the condensation of non-converted bio-oil compounds.

The non-condensable gaseous products were analyzed on-line in a micro GC (Varian 4900), and in this case the samples were taken after the condensation and filtering processes (see Fig. 1). The micro GC was equipped with four modules, namely, Molecular sieve 5, Porapak (PPQ), CPSil and Plot Alumina, with the four channels being equipped with thermal conductivity detectors (TCD).

2.7. Reaction indexes

In order to evaluate the performance of the different catalyst prepared, conversion and individual product yields were considered as the key reaction indexes. All the reaction indexes are based on the feed into the reforming step, i.e. pyrolysis volatiles (gas and bio-oil) and not on the biomass fed into the pyrolysis step. The reforming conversion has been defined similarly as the carbon conversion efficiency commonly used in the gasification processes, i.e., the ratio between the moles of C recovered in the gaseous product and those fed into the reforming step. Accordingly, the carbon contained in the char produced in the pyrolysis step was not considered for calculating the conversion in the reforming step, given that this product was removed from the process prior to the reforming step.

$$X = \frac{C_{gas}}{C_{volatiles}}100 \qquad (1)$$
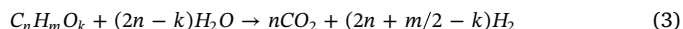
Similarly, the yield of C containing individual compounds has been based on the biomass pyrolysis volatile stream:

$$Y_i = \frac{F_i}{F_{volatiles}}100 \qquad (2)$$

where F$_i$ and F$_{volatiles}$ are the molar flow rates of product i and pyrolysis volatiles, respectively, both given in C units contained. The bio-oil yield

was also calculated in the reforming step by considering the carbon units contained in the non-reformed oxygenated compounds in the stream leaving the reforming step.

The hydrogen yield was determined as a percentage of the maximum allowable by stoichiometry, which accounts for the H$_2$ coming from both the pyrolysis volatiles and the steam. It is to note that the char was not considered in this calculation because it was not fed into the reforming step. The following stoichiometry was considered:

$$C_nH_mO_k + (2n - k)H_2O \rightarrow nCO_2 + (2n + m/2 - k)H_2 \qquad (3)$$

$$Y_{H_2} = \frac{F_{H_2}}{F_{H_2}^0}100 \qquad (4)$$

where F$_{H2}$ and F°$_{H2}$ are the H$_2$ molar flow rates obtained in the run and the maximum allowable by stoichiometry.

H$_2$ production was calculated as the mass of H$_2$ produced per biomass mass unit fed into the pyrolysis step:

$$P_{H_2} = \frac{m_{H_2}}{m_{Biomass}^0}100 \qquad (5)$$

3. Results

3.1. Catalyst characterization

The textural properties of both the original supports and the prepared catalysts were determined by means of N$_2$ adsorption-desorption and are summarized in Table 2. These properties play a remarkable role on the reforming catalysts performance, given that a high surface area greatly improves the dispersion of the active phase [61]. As observed in Table 2, the supports used are mesoporous materials, with an average pore size ranging from 20 to 250 Å. In the case of SiO$_2$ support, a porous structure with considerable microporosity, low average pore size (21 Å) and high BET surface area (703 m^2 g^{-1}) were observed, which leads to significant micropore volume. On the other hand, MgO had a poor porous structure, with a very low surface area of only 1 m^2 g^{-1}. The other supports (Al$_2$O$_3$, TiO$_2$ and ZrO$_2$) have similar features, with BET surface areas ranging from 90 to 150 m^2 g^{-1} and average pore sizes from 115 to 175 Å.

Once Ni impregnation had been carried, significant differences were observed in the catalysts surface properties compared to those of the supports. Thus, the surface area and pore volume of the impregnated catalysts were significantly reduced, except for MgO. The decrease in surface area after impregnation is attributed to the blockage of the support pores by nickel species, which make them inaccessible for N$_2$ adsorption [62]. In addition, the average pore sizes of Ni/TiO$_2$ and Ni/ZrO$_2$ catalysts undergo a considerable increase, which suggests that Ni was mainly deposited on the finest pores. However, the location of Ni in

Table 2
Composition and properties of the catalysts and original supports.

Catalyst	Metal content wt %	S$_{BET}$ m^2/g	V$_{pore}$ cm^3/g	d$_{pore}$ Å	d$_{M\ XRD}$[a] nm	Ni dispersion[b] %
Al$_2$O$_3$	–	87	0.38	173	–	–
SiO$_2$	–	703	0.16[c]/0.36	21	–	–
MgO	–	1	0.00	28	–	–
TiO$_2$	–	154	0.44	114	–	–
ZrO$_2$	–	97	0.30	122	–	–
Ni/Al$_2$O$_3$	9.79	76	0.32	166	10.2	10
Ni/SiO$_2$	9.55	429	0.07[c]/0.22	21	11.1	9
Ni/MgO	9.79	6	0.02	152	n.d	n.d
Ni/TiO$_2$	9.95	22	0.14	259	49.2	2
Ni/ZrO$_2$	9.51	34	0.22	255	28.5	4

[a] Calculated from the full width at half height of the Ni (2 0 0) diffraction peak at 2θ = 52° in the XRD using the Scherrer equation.
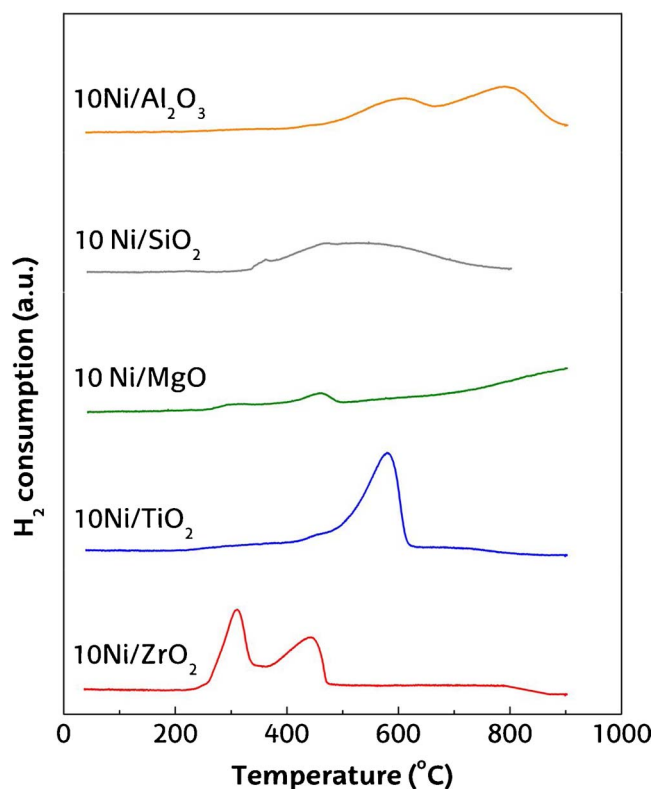[b] Dispersion calculated as (97.1 nm)/(Particle size of Ni (nm)) [50].
[c] Micropore volume.

Fig. 2. TPR profiles of Ni based catalysts.

Fig. 3. XRD patterns of the reduced catalyst. Crystalline phases: (●) Ni, (▲) Al_2O_3, (▼) SiO_2, (●) NiO/MgO, (A) TiO_2 (Anatase), (R) TiO_2 (Rutile), (★) ZrO_2.

the case of MgO is mainly external due to the poor porous structure of this material. In fact, the selective impregnation of Ni on the catalyst external surface led to an increase in its surface area, which is consistent with the trend reported for Ni impregnation on supports of low porosity [37,63].

Table 2 also shows the Ni load, averaged crystallite size and dispersion. According to the XRF analysis, the metal content of the catalysts was very similar to the nominal loading (10 wt%), and it can therefore be concluded that the wet impregnation method is suitable for the synthesis of catalysts. The dispersion values are in general low, which is due the low surface area of the support and the relatively high metal content [38]. Accordingly, better dispersion values were obtained for the catalysts with higher surface area, i.e., for Ni/SiO_2 and Ni/Al_2O_3. It should be noted that the Ni particle size and dispersion were not determined for the Ni/MgO catalyst because the diffraction peak associated with Ni was not observed in the XRD analysis due to the strong metal-support interaction.

Fig. 2 shows the TPR profiles of the Ni catalysts. As observed in the figure, these profiles not only depend on the nature of the metal function, but the supports also play an important role in the reduction of the catalysts. Additionally, the TPR analysis has been complemented with the XRD technique (Fig. 3), whereby the possible reducible metal species that make up the catalyst may be identified.

Thus, different NiO precursors are present in the catalysts and are reduced at specific temperature ranges. The Ni/Al_2O_3 catalyst shows two main peaks, and the reduction of weakly interacting NiO is also observed prior to the first peak [37]. Given the high temperature corresponding to the first peak (620 °C), it should be associated with the reduction of highly dispersed and strongly interacting NiO [64]. The peak located above 780 °C is attributed to Ni atoms that have migrated into the Al_2O_3 support to form a very stable $NiAl_2O_4$ spinel-type phase [37,64,65].

Three peaks are observed in the TPR profiles of Ni/SiO_2, which are associated with the reduction of different nickel species. Two small shoulders appear at about 360 °C and 480 °C and a main broad peak at
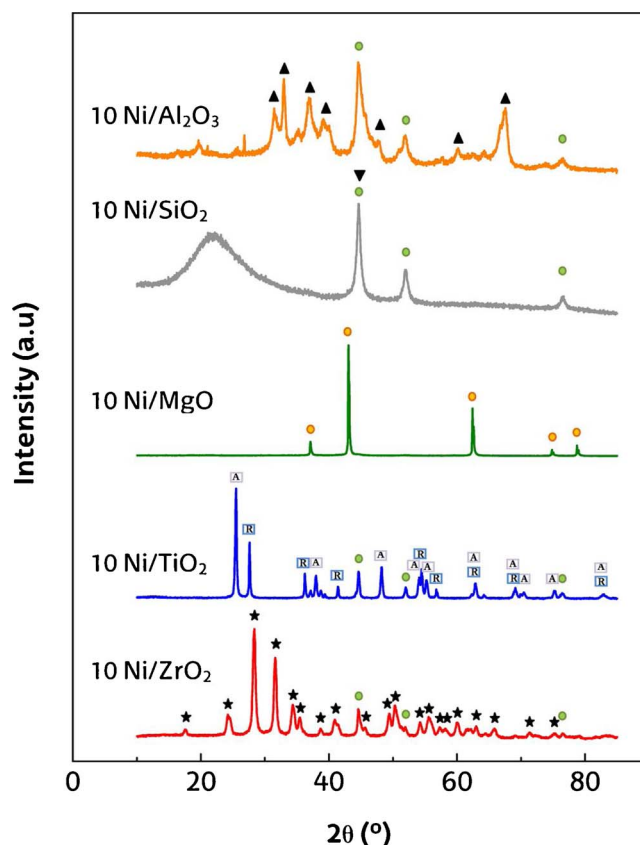
550 °C. The first two reduction peaks located between 350 and 500 °C are due to the reduction of nickel species weakly or moderately interacting with the support. A very broad peak situated above 550 °C is attributable to the reduction of nickel species interacting strongly with the silica support or to hardly reducible nickel silicate, which may be formed via reaction of small nickel oxide particles with silica [66,67].

In the case of Ni/MgO catalysts, two reduction peaks at around 310 °C and 480 °C are observed. A third peak seems to be located at a temperature above 700 °C [68,69]. The first one should be assigned to the reduction of NiO located on the MgO surface, whereas the second one at 480 °C should be attributed to certain Ni^{2+} ions arranged in square-pyramidal coordination on the external layers of the MgO structure [68]. Finally, the formation of NiO–MgO bulk solid solution leads to the oxidized form of Ni, which is reducible above 700 °C. In fact, the presence of this solution has also been observed in the XRD analysis when the catalyst was reduced at 710 °C.

In the catalyst supported on TiO_2, a small peak centred at 480 °C and a higher one at 580 °C are observed in the TPR patterns. According to Nichele et al. [70], the peak centred at 480 °C is due to NiO species strongly interacting with the support, whereas the reduction peak appearing between 550 and 700 °C, should be assigned to bulk $NiTiO_3$. It should be noted that Ni/TiO_2 catalyst can be fully reduced at 650 °C.

The temperature reduction profiles for Ni/ZrO_2 showed two main peaks located at 300 °C and 450 °C. The lower temperature peak is assigned to the reduction of the relatively free NiO species, whereas the higher one is attributed to the reduction of NiO species, which have low specific interaction with the ZrO_2 support [71].

The X-ray diffraction patterns of the catalysts reduced at 710 °C for 4 h are shown in Fig. 3. As observed, diffraction lines appear for catalysts Ni/Al_2O_3, Ni/SiO_2, Ni/TiO_2 and Ni/ZrO_2 at 2θ = 44°, 52° and 76°, which are due to crystalline phases of Ni corresponding to the planes (1 1 1), (2 0 0) and (2 2 0), respectively [72,73]. The NiO crystalline phase

was not detected in the reduced samples of the previously mentioned supports, which is evidence of full reduction of this species. However, for the MgO supported catalyst, the XRD spectrum shows a complete solid solution of NiO in MgO in all the diffraction peaks. The formation of NiO–MgO solid solution is consistent with the TPR results, in which a low reduction extent was observed, indicating a clear strong interaction between the metal and the support [74].

Poor crystalline properties of γ-Al$_2$O$_3$ were observed at 2θ = 45° and 67° in the Ni/Al$_2$O$_3$ catalyst. The XRD results do not show the diffraction peak related to NiAl$_2$O$_4$, which should be reflected at 2θ = 19°, 45° and 60° [75]. The diffraction patterns obtained showed peaks at these angles ascribed to γ-Al$_2$O$_3$ support, which based on the TPR profiles may overlap the spinel.

The results for Ni/SiO$_2$ catalyst show a broad diffraction peak at 2θ between 20° and 30° attributed to the peak of the siliceous material.

The anatase phase in Ni/TiO$_2$ was partially converted into rutile after reduction (XRD of calcined catalyst is not shown). The reflections of rutile phase appeared at 2θ = 27°, 36°, 41°, 54° and 56°. The absence of reflections characteristic to nickel titanate suggest its reduction to Ni [76].

The XRD spectrum of Ni/ZrO$_2$ catalyst shows characteristic diffraction peaks at 2θ = 28° and 31° ascribed to pure monoclinic phase (m-ZrO$_2$) [77]. The diffraction peaks characteristic to the tetragonal phase (t-ZrO$_2$) at 2θ = 34°, 45° and 60° [78] have also been observed.

In order to estimate the dispersion, the metal particle size can be determined using the Scherrer equation in the peak at 2θ = 52°, which is assigned to the diffraction of Ni(2 0 0) in XRD patterns. The results are summarized in Table 2. The Ni particle size varies with the support and decreases according to the following order: Ni/TiO$_2$ > Ni/ZrO$_2$ > Ni/SiO$_2$ > Ni/Al$_2$O$_3$. The estimation of Ni particle size for Ni/MgO is not possible due to the strong interaction between the active phase and the support.

3.2. Biomass pyrolysis results (first step)

In the pyrolysis step, the char produced was continuously removed from the pyrolysis reactor while pyrolysis volatiles were transferred to the second reactor for their reforming. The pyrolysis step was carried out under steam environment, with the steam required in the reforming step being introduced in the pyrolysis reactor, where it plays the role of a fluidizing agent. As proven in previous papers, steam at 500 °C has hardly any influence on biomass pyrolysis product distribution [19], i.e., the results are similar to those obtained in the same reactor and using the same biomass (pine wood sawdust) under inert conditions (N$_2$) [45].

Continuous char removal in the flash pyrolysis step is an interesting feature of the CSBR [45,46], given that secondary reactions of pyrolysis volatiles on the char surface are minimised [15]. Moreover, the fast removal of the char improves the quality of the char, which is a point of especial interest for its subsequent valorisation [79,80].

As observed in Table 3, the main volatile product obtained in the pyrolysis step was bio-oil, with its yield being 75 wt%, which is evidence of the excellent characteristics of the CSBR for fast pyrolysis of solid wastes [81]. The bio-oil obtained is a complex mixture of oxygenated compounds of different nature, including phenols (16.5 wt%), ketones (6.4%), saccharides (4.5%), furans (3.3%), acids (2.7%), alcohols (2.0%) and aldehydes (1.9%). In addition, a water yield of around 25 wt% was also obtained [45]. The non-condensable gaseous products obtained in the pyrolysis step (7.3% yield) were mainly made up of CO and CO$_2$, with those of CH$_4$ and other hydrocarbons being low [45].
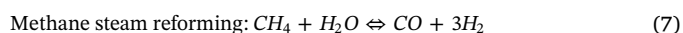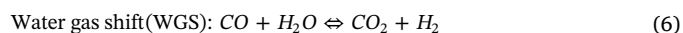
Table 3
Product distribution in the pyrolysis step performed at 500 °C.

Compound	Yield (wt %)
Gas	**7.3**
CO	3.38
CO$_2$	3.27
CH$_4$	0.36
Hydrocarbons (C$_2$-C$_4$)	0.3
H$_2$	0.04
Bio-oil	**75.3**
Acids	2.73
Aldehydes	1.93
Alcohols	2
Ketones	6.37
Phenols	16.49
Furans	3.32
Saccharides	4.46
Water	25.36
Char	**17.3**

### 3.3. Performance of steam reforming catalysts (second step)

The influence the support contained in Ni based catalysts has on catalyst activity has been analyzed. Thus, the reaction indexes defined in section 2.7 (conversion, individual product yields and H$_2$ production) have been monitored for the different catalysts tested, and gas fraction composition and gas production have also been determined. In order to evaluate the performance of the different catalyst, the following reactions have been considered in the reforming reactor:

The steam reforming of oxygenates, Eq. (3).

$$Water\ gas\ shift\,(WGS): CO + H_2O \Leftrightarrow CO_2 + H_2 \qquad (6)$$

$$Methane\ steam\ reforming: CH_4 + H_2O \Leftrightarrow CO + 3H_2 \qquad (7)$$

$$Cracking\,(secondary\ reaction): C_nH_mO_k \rightarrow oxygenates + hydrocarbons + CH_4 + CO + CO_2 \qquad (8)$$

The products obtained at the outlet of the reforming reactor have been grouped into two fractions: the gaseous products and the liquids ones (non-converted bio-oil). The main gaseous products obtained in the reforming step are H$_2$, CO$_2$ and CO, with low concentrations of CH$_4$ and light hydrocarbons (C$_2$-C$_4$) being also detected.

Fig. 4 shows the conversions obtained with the different catalysts, using space times of 10 and 20 g$_{cat}$ min g$_{volatiles}$$^{-1}$. For the highest space
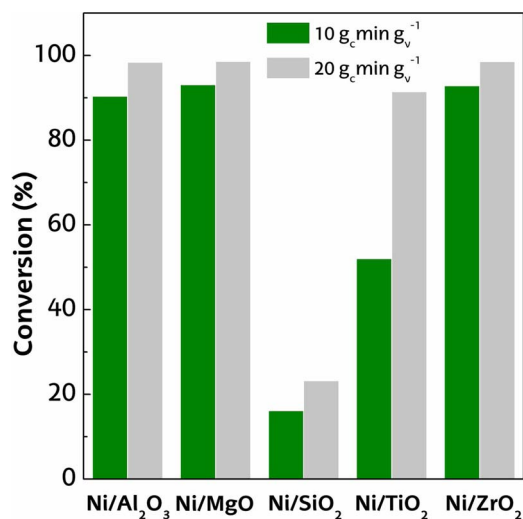
Fig. 4. Conversion in the in line reforming of pyrolysis volatiles on different catalysts with space times of 10 and 20 g$_{cat}$ min g$_{volatiles}$$^{-1}$.

time studied, almost full conversion (> 98%) was attained for Ni/Al_2O_3, Ni/MgO and Ni/ZrO_2 catalysts. In the case of Ni/TiO_2 catalyst, conversion was 91%, whereas Ni/SiO_2 had a low reforming activity, with conversion being 23%. On the other hand, the experimental runs performed with a space time of 10 g_{cat} min $g_{volatiles}^{-1}$ provided more interesting results regarding catalyst activity, given that this space time is clearly below the one corresponding to equilibrium.

The activity of Ni reforming catalysts has been usually related to the capacity of the support to provide a suitable metal dispersion [13,38]. However, Ni/SiO_2 catalyst showed an adequate Ni dispersion and low crystalline size, and therefore the poor results obtained using this catalyst should be related to the bulky nature of biomass pyrolysis derived molecules. Indeed, SiO_2 support is characterized by a fine microporous structure (see Table 2), and therefore the accessibility and diffusion limitations of bio-oil molecules to Ni sites may explain the low reforming activity observed. The Ni/TiO_2 catalyst also showed a poor performance compared to the other ones studied, and the low Ni dispersion may be responsible for the limited activity of this catalyst. In spite of the low surface area and metal dispersion attained when MgO support is used, and the strong metal-support interaction hindering Ni reducibility [82], this catalyst has shown a suitable activity, with the conversion obtained for a space time of 10 g_{cat} min $g_{volatiles}^{-1}$ being of the same order (around 90%) as that observed for more porous supports, such as Al_2O_3 and ZrO_2. The more plausible explanation is that Ni is located mainly on the external surface of the support, which makes it highly accessible to pyrolysis volatiles and accordingly improves catalyst activity. Miyazama et al. [38] studied the performance of different Ni supported catalysts in the reforming of biomass derived tar and, similarly as in this study, they obtained the best performance for Ni/Al_2O_3 and Ni/ZrO_2 catalysts. However these authors reported a low activity for Ni/MgO catalyst, i.e., significantly lower than for Ni/TiO_2.

Fig. 5 shows the yields of the individual products obtained on the catalysts studied, with space times of 10 (Fig. 5a) and 20 g_{cat} min $g_{volatiles}^{-1}$ (Fig. 5b). As observed, higher H_2 yields were obtained for Ni/Al_2O_3, Ni/ZrO_2 and Ni/MgO catalysts, with the yields being above 80 and 90% for the space times of 10 (Fig. 5a) and 20 g_{cat} min $g_{volatiles}^{-1}$, respectively. For all the catalysts studied, an increase in space time promotes both steam reforming (Eq. (3)) and WGS reaction (Eq. (6)), which leads to an increase in H_2 and CO_2 yields and a decrease in those of gaseous hydrocarbons and non-converted bio-oil. Interestingly, the yield of non-converted bio-oil is almost negligible for Ni/Al_2O_3, Ni/ZrO_2 and Ni/MgO catalysts. Moreover, a further increase in space time allows for fully converting the biomass tar, which means a great advantage of the strategy studied here over the conventional

gasification for the production of a suitable gaseous stream for industrial applications [19].

Fig. 6 shows the composition of the gas produced with the different catalysts and space times studied. As observed, the influence space time has on the gas composition is less pronounced than on individual product yields. In fact, similar gas compositions were observed for highly active catalyst (Ni/Al_2O_3, Ni/ZrO_2 and Ni/MgO) using space times of 10 and 20 g_{cat} min $g_{volatiles}^{-1}$. It should be noted that the concentration of cracking compounds, such as methane and light hydrocarbons, is very low even under low conversions, as is the case of Ni/TiO_2 and Ni/SiO_2 catalysts. This fact is related to the moderate temperature used (600 °C) and to the relatively short residence time in the reactor.

The results corresponding to the production of H_2 and gaseous stream are clear evidence of the overall pyrolysis-reforming conversion efficiency, given that both reaction indexes are based on the biomass mass unit in the feed. This definition of reaction indices allows an easy comparison of the results obtained here with other routes aimed at H_2 rich gas production from biomass, such as bio-oil reforming or steam gasification (see Table 4). Thus, the results obtained in a previous study in the same experimental unit and under the same experimental conditions (temperature, space time and S/B ratio) on a commercial catalyst of Ni/Al_2O_3 doped with Ca (11.17 wt% H_2 production and 1.89 $m^3 kg^{-1}$ gas production [19]) are slightly better than those reported here for the best catalysts, i.e., Ni/Al_2O_3 and Ni/ZrO_2. These results are explained by the higher Ni content of the commercial catalyst, i.e., 11.34% instead of 10% corresponding to those prepared in this study. Xiao et al. [17,18] reported H_2 production values of the order of 10 wt% in the pyrolysis-reforming (fluidized bed/fixed bed continuous unit) of pine wood chips on a Ni/coal char catalyst at similar reforming temperatures. The maximum H_2 production obtained by Ma et al. [20] in a three-step process (biomass pyrolysis in a fluidized bed reactor, gasification in an entrained flow reactor and reforming in a fixed bed) was 7.6 wt% at the highest reforming temperature studied (850 °C) on a Ni/MgO commercial catalyst. The results obtained by the research group headed by Prof. Williams in a two fixed bed reactor system operating in batch regime are clearly lower, with values being in the range from 2 to 3 wt% on Ni/Al_2O_3 and Ni/$CaAlO_x$ catalysts [62,83]. The H_2 productions obtained in steam gasification processes are in general considerably lower than those reported in the pyrolysis-reforming strategy, with values being below 8 wt% even using suitable primary catalysts and under optimum operating conditions. Similarly, gas production values are in the 0.9 to 1.2 $Nm^3 kg_{biomass}^{-1}$ range, which are far from the values obtained in the pyrolysis-reforming process [84–86]. The indirect route of bio-oil reforming is an alternative strategy to the
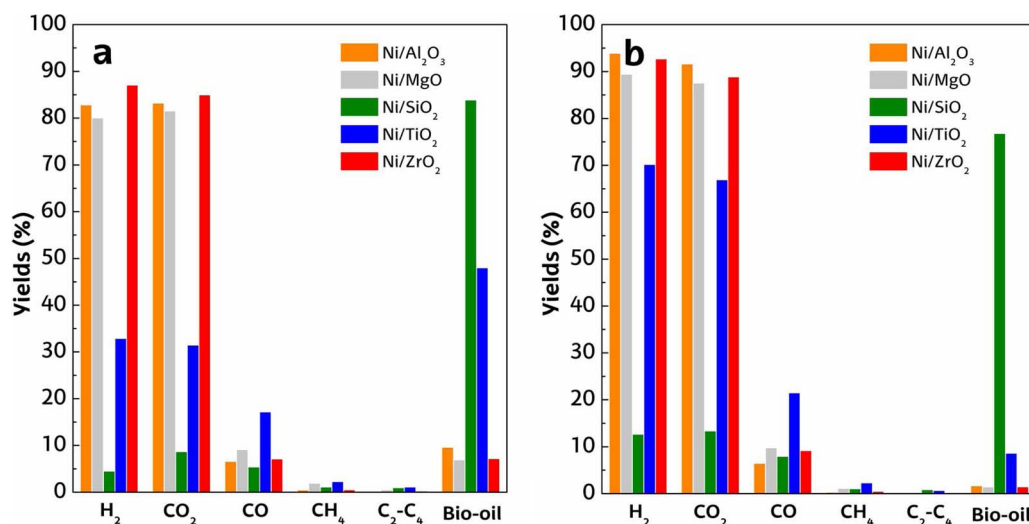

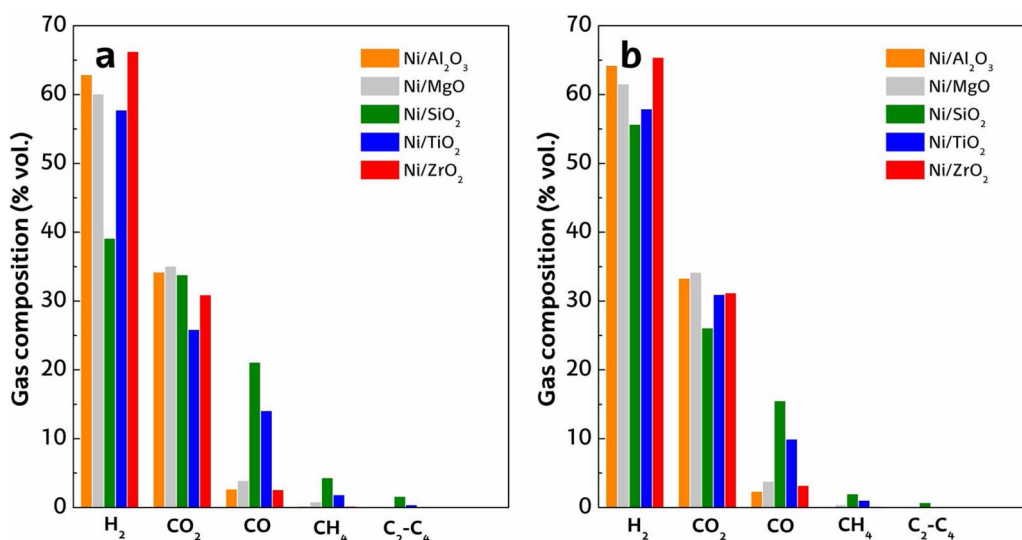**Fig. 5.** Influence of catalyst support on the individual product yields for space times of 10 (Fig. 5a) and 20 g_{cat} min $g_{volatiles}^{-1}$ (Fig. 5b).

Fig. 6. Influence of Ni support on the gaseous stream composition for space times of 10 (Fig. 6a) and 20 g_{cat} min $g_{volatiles}^{-1}$ (Fig. 6b).

Table 4
H_2 and gas productions obtained on the reforming catalysts used in this study and in a previous one on a Ni commercial catalyst [19] for a space time of 20 g_{cat} min $g_{volatiles}^{-1}$.

	Ni/Al$_2$O$_3$	Ni/MgO	Ni/SiO$_2$	Ni/TiO$_2$	Ni/ZrO$_2$	Ni/commercial
H$_2$ production (wt%)	10.17	9.08	1.64	7.21	10.73	11.17
Gas production (Nm^3 kg^{-1})	1.77	1.65	0.33	1.4	1.84	1.89

pyrolysis-reforming process, in which H_2 production values are usually in the 10 to 15 wt% range [10,36,87,88]. Furthermore, it should be noted that these productions are based on the bio-oil mass unit and not on the original biomass mass unit, with the bio-oil yield being below 75% even under the optimum pyrolysis conditions [15,89].

4. Conclusions

The continuous reforming of biomass fast pyrolysis volatiles in a CSBR-FBR system has proven to be a suitable process for the direct H_2 production from biomass. The influence of the support on Ni based catalysts has been studied in the in line reforming of biomass fast pyrolysis volatiles, and remarkable differences have been observed amongst the prepared catalysts. The Ni/Al$_2$O$_3$ and Ni/ZrO$_2$ catalysts showed the best activity, which is related to the suitable physical properties of the support favouring a proper metal dispersion. Thus, full conversion of biomass pyrolysis volatiles was obtained for a space time of 20 g_{cat} min $g_{volatiles}^{-1}$, with hydrogen production being above 10 wt % for both catalysts. The low dispersion observed in the Ni/TiO$_2$ catalyst leads to poorer activity, with H_2 production being 7.2 wt%. Although SiO$_2$ was the support with higher surface area and allowed for a high Ni dispersion, its fine porous structure hindered the access of bio-oil bulky molecules, leading to a markedly reduced activity. Finally, the Ni/MgO catalyst with low dispersion and Ni reducibility showed an unexpected suitable activity, with H_2 production being 9.0 wt%. This result is related to the fact that Ni is mainly deposited on the external surface of the support, which improves the accessibility of bulky oxygenate molecules.

Acknowledgments

References

[1] A. Sanna, Bioenergy Res. 7 (2014) 36–47.
[2] R. Parajuli, T. Dalgaard, U. Jørgensen, A.P.S. Adamsen, M.T. Knudsen, M. Birkved, M. Gylling, J.K. Schjørring, Renew. Sustain. Energy Rev. 43 (2015) 244–263.
[3] J.A. Melero, J. Iglesias, A. Garcia, Energy Environ. Sci. 5 (2012) 7393–7420.
[4] H. Balat, E. Kirtay, Int. J. Hydrogen Energy 35 (2010) 7416–7426.
[5] A.A. Ahmad, N.A. Zawawi, F.H. Kasim, A. Inayat, A. Khasri, Renew. Sustain. Energy Rev. 53 (2016) 1333–1347.
[6] S.K. Sansaniwal, K. Pal, M.A. Rosen, S.K. Tyagi, Renew. Sustain. Energy Rev. 72 (2017) 363–384.
[7] P.J. Woolcock, R.C. Brown, Biomass Bioenergy 52 (2013) 54–84.
[8] W. Nabgan, T.A. Tuan Abdullah, R. Mat, B. Nabgan, Y. Gambo, M. Ibrahim, A. Ahmad, A.A. Jalil, S. Triwahyono, I. Saeh, Renew. Sustain. Energy Rev. 79 (2017) 347–357.
[9] J. Chen, J. Sun, Y. Wang, Ind. Eng. Chem. Res. 56 (2017) 4627–4637.
[10] A. Remiro, B. Valle, A.T. Aguayo, J. Bilbao, A.G. Gayubo, Energy Fuels 27 (2013) 7549–7559.
[11] A.A. Lemonidou, P. Kechagiopoulos, E. Heracleous, S. Voutetakis, The Role of Catalysis for the Sustainable Production of Bio-Fuels and Bio-Chemicals, (2013), pp. 467–493.
[12] A. Remiro, B. Valle, B. Aramburu, A.T. Aguayo, J. Bilbao, A.G. Gayubo, Ind. Eng. Chem. Res. 52 (2013) 17087–17098.
[13] R. Trane, S. Dahl, M.S. Skjoth-Rasmussen, A.D. Jensen, Int. J. Hydrogen Energy 37 (2012) 6447–6472.
[14] F. Bimbela, J. Ábrego, R. Puerta, L. García, J. Arauzo, Appl. Catal. B 209 (2017) 346–357.
[15] A.V. Bridgwater, Biomass Bioenergy 38 (2012) 68–94.
[16] B. Puértolas, T.C. Keller, S. Mitchell, J. Pérez-Ramírez, Appl. Catal. B 184 (2016) 77–86.
[17] X. Xiao, X. Meng, D.D. Le, T. Takarada, Bioresour. Technol. 102 (2011) 1975–1981.
[18] X. Xiao, J. Cao, X. Meng, D.D. Le, L. Li, Y. Ogawa, K. Sato, T. Takarada, Fuel 103 (2013) 135–140.
[19] A. Arregi, G. Lopez, M. Amutio, I. Barbarias, J. Bilbao, M. Olazar, RSC Adv. 6 (2016) 25975–25985.
[20] Z. Ma, S. Zhang, D. Xie, Y. Yan, Int. J. Hydrogen Energy 39 (2014) 1274–1279.
[21] L. Wang, D. Li, M. Koike, H. Watanabe, Y. Xu, Y. Nakagawa, K. Tomishige, Fuel 112 (2013) 654–661.
[22] J. Cao, P. Shi, X. Zhao, X. Wei, T. Takarada, Fuel Process. Technol. 123 (2014) 34–40.
[23] T. Namioka, A. Saito, Y. Inoue, Y. Park, T. Min, S. Roh, K. Yoshikawa, Appl. Energy 88 (2011) 2019–2026.
[24] I. Barbarias, G. Lopez, J. Alvarez, M. Artetxe, A. Arregi, J. Bilbao, M. Olazar, Chem. Eng. J. 296 (2016) 191–198.
[25] I. Barbarias, G. Lopez, M. Artetxe, A. Arregi, L. Santamaria, J. Bilbao, M. Olazar, J. Anal. Appl. Pyrolysis 122 (2016) 502–510.
[26] J.C. Acomb, C. Wu, P.T. Williams, Appl. Catal. B 147 (2014) 571–584.

[27] A. Arregi, M. Amutio, G. Lopez, M. Artetxe, J. Alvarez, J. Bilbao, M. Olazar, Energy Convers. Manage. 136 (2017) 192–201.
[28] J. Alvarez, S. Kumagai, C. Wu, T. Yoshioka, J. Bilbao, M. Olazar, Int. J. Hydrogen Energy 39 (2014) 10883–10891.
[29] S. Czernik, R. French, Int. J. Hydrogen Energy 39 (2014) 744–750.
[30] R. Trane-Restrup, A.D. Jensen, Appl. Catal. B. 165 (2015) 117.
[31] M. Ni, D.Y.C. Leung, M.K.H. Leung, Int. J. Hydrogen Energy 32 (2007) 3238.
[32] D. Li, L. Wang, M. Koike, Y. Nakagawa, K. Tomishige, Appl. Catal. B 102 (2011) 528–538.
[33] R. Trane-Restrup, S. Dahl, A.D. Jensen, Int. J. Hydrogen Energy 38 (2013) 15105–15118.
[34] M.L. Ang, U. Oemar, Y. Kathiraser, E.T. Saw, C.H.K. Lew, Y. Du, A. Borgna, S. Kawi, J. Catal. 329 (2015) 130–143.
[35] S. Li, J. Gong, Chem. Soc. Rev. 43 (2014) 7245–7256.
[36] F. Seyedeyn Azad, J. Abedi, E. Salehi, T. Harding, Chem. Eng. J. 180 (2012) 145–150.
[37] I. García-García, E. Acha, K. Bizkarra, J. Martínez de Ilarduya, J. Requies, J.F. Cambra, Int. J. Hydrogen Energy 40 (2015) 14445–14455.
[38] T. Miyazawa, T. Kimura, J. Nishikawa, S. Kado, K. Kunimori, K. Tomishige, Catal. Today 115 (2006) 254–262.
[39] A.H. Braga, E.R. Sodré, J.B.O. Santos, C.M. de Paula Marques, J.M.C. Bueno, Appl. Catal. B 195 (2016) 16–28.
[40] M. Inaba, K. Murata, M. Saito, I. Takahara, Energy Fuels 20 (2006) 432–438.
[41] S. Zhang, X. Li, Q. Li, Q. Xu, Y. Yan, J. Anal, Appl. Pyrolysis 92 (2011) 158–163.
[42] H. Li, Q. Xu, H. Xue, Y. Yan, Renew. Energy 34 (2009) 2872–2877.
[43] Q.M.K. Waheed, P.T. Williams, Energy Fuels 27 (2013) 6695–6704.
[44] P. Lan, L.H. Lan, T. Xie, A.P. Liao, Energy Sour. Recovery Util. Environ. Eff. 36 (2014) 242–249.
[45] M. Amutio, G. Lopez, M. Artetxe, G. Elordi, M. Olazar, J. Bilbao, Resour. Conserv. Recycl. 59 (2012) 23–31.
[46] J. Alvarez, G. Lopez, M. Amutio, J. Bilbao, M. Olazar, Fuel 128 (2014) 162–169.
[47] M. Amutio, G. Lopez, R. Aguado, M. Artetxe, J. Bilbao, M. Olazar, Fuel 95 (2012) 305–311.
[48] L. An, C. Dong, Y. Yang, J. Zhang, L. He, Renew. Energy 36 (2011) 930–935.
[49] J. Sehested, J.A.P. Gelten, S. Helveg, Appl. Catal. A 309 (2006) 237–246.
[50] D.G. Mustard, C.H. Bartholomew, J. Catal. 67 (1981) 186–206.
[51] J. Alvarez, M. Amutio, G. Lopez, J. Bilbao, M. Olazar, Fuel 159 (2015) 810–818.
[52] M. Artetxe, G. Lopez, M. Amutio, G. Elordi, J. Bilbao, M. Olazar, Ind. Eng. Chem. Res. 52 (2013) 10637–10645.
[53] M. Artetxe, G. Lopez, M. Amutio, I. Barbarias, A. Arregi, R. Aguado, J. Bilbao, M. Olazar, Waste Manage. 46 (2015) 126–133.
[54] G. Lopez, J. Alvarez, M. Amutio, N.M. Mkhize, B. Danon, P. van der Gryp, J.F. Görgens, J. Bilbao, M. Olazar, Energy Convers. Manage. 142 (2017) 523–532.
[55] G. Lopez, M. Olazar, R. Aguado, J. Bilbao, Fuel 89 (2010) 1946–1952.
[56] A. Remiro, B. Valle, A.T. Aguayo, J. Bilbao, A.G. Gayubo, Fuel Process. Technol. 115 (2013) 222–232.
[57] A. Erkiaga, G. Lopez, I. Barbarias, M. Artetxe, M. Amutio, J. Bilbao, M. Olazar, J. Anal, Appl. Pyrolysis 116 (2015) 34–41.
[58] J. Remón, F. Broust, G. Volle, L. García, J. Arauzo, Int. J. Hydrogen Energy 40 (2015) 5593–5608.
[59] J.A. Moulijn, A.E. Van Diepen, F. Kapteijn, Wiley-VCH (Ed.), Handbook of Heterogeneous Catalysis, 2010, pp. 1–17.
[60] J. Alvarez, M. Amutio, G. Lopez, I. Barbarias, J. Bilbao, M. Olazar, Chem. Eng. J. 273 (2015) 173–183.
[61] V. Nichele, M. Signoretto, F. Menegazzo, A. Gallo, G. Dal Santo, G. Cruciani, G. Cerrato, Appl. Catal. B 111–112 (2012) 225–232.
[62] F. Chen, C. Wu, L. Dong, A. Vassallo, P.T. Williams, J. Huang, Appl. Catal. B 183 (2016) 168–175.
[63] X. Yang, S. Xu, H. Xu, X. Liu, C. Liu, Catal. Commun. 11 (2010) 383–386.
[64] R.M. Navarro, R. Guil-Lopez, A.A. Ismail, S.A. Al-Sayari, J.L.G. Fierro, Catal. Today 242 (2015) 60–70.
[65] F. Seyedeyn-Azad, E. Salehi, J. Abedi, T. Harding, Fuel Process. Technol. 92 (2011) 563–569.
[66] Y. Pan, C. Liu, P. Shi, J. Power Sources 176 (2008) 46–53.
[67] F. Huang, R. Wang, C. Yang, H. Driss, W. Chu, H. Zhang, J. Energy Chem. 25 (2016) 709–719.
[68] S. Freni, S. Cavallaro, N. Mondello, L. Spadaro, F. Frusteri, Catal. Commun. 4 (2003) 259–268.
[69] T. Furusawa, T. Sato, H. Sugito, Y. Miura, Y. Ishiyama, M. Sato, N. Itoh, N. Suzuki, Int. J. Hydrogen Energy 32 (2007) 699–704.
[70] V. Nichele, M. Signoretto, F. Menegazzo, I. Rossetti, G. Cruciani, Int. J. Hydrogen Energy 39 (2014) 4252–4258.
[71] F. Pompeo, N.N. Nichio, M.M.V.M. Souza, D.V. Cesar, O.A. Ferretti, M. Schmal, Appl. Catal. A 316 (2007) 175–183.
[72] International Centre for Diffraction Data. (2003).
[73] R.D. Tilley, D.A. Jefferson, J. Mater. Chem. 12 (2002) 3809–3813.
[74] A. Djaidja, S. Libs, A. Kiennemann, A. Barama, Catal. Today 113 (2006) 194–200.
[75] B. Valle, B. Aramburu, A. Remiro, J. Bilbao, A.G. Gayubo, Appl. Catal. B 147 (2014) 402–410.
[76] K.J.A. Raj, M.G. Prakash, R. Mahalakshmy, T. Elangovan, B. Viswanathan, Catal. Sci. Technol. 2 (2012) 1429–1436.
[77] S. Li, M. Li, C. Zhang, S. Wang, X. Ma, J. Gong, Int. J. Hydrogen Energy 37 (2012) 2940–2949.
[78] Q. Liu, X. Dong, X. Mo, W. Lin, J. Nat. Gas Chem. 17 (2008) 268–272.
[79] C.M. Dominguez, P. Ocon, A. Quintanilla, J.A. Casas, J.J. Rodriguez, Appl. Catal. B 140–141 (2013) 663–670.
[80] J. Alvarez, G. Lopez, M. Amutio, J. Bilbao, M. Olazar, Bioresour. Technol. 170 (2014) 132–137.
[81] G. Lopez, M. Artetxe, M. Amutio, J. Bilbao, M. Olazar, Renew. Sustain. Energy Rev. 73 (2017) 346–368.
[82] K. Tomishige, Y.- Chen, K. Fujimoto, J. Catal. 181 (1999) 91–103.
[83] A.K. Olaleye, K.J. Adedayo, C. Wu, M.A. Nahil, M. Wang, P.T. Williams, Fuel 137 (2014) 364–374.
[84] S. Koppatz, C. Pfeifer, H. Hofbauer, Chem. Eng. J. 175 (2011) 468–483.
[85] A. Erkiaga, G. Lopez, M. Amutio, J. Bilbao, M. Olazar, Chem. Eng. J. 237 (2014) 259–267.
[86] S. Rapagna, M. Virginie, K. Gallucci, C. Courson, M. Di Marcello, A. Kiennemann, P.U. Foscolo, Catal. Today 176 (2011) 163–168.
[87] C. Wu, Q. Huang, M. Sui, Y. Yan, F. Wang, Fuel Process. Technol. 89 (2008) 1306–1316.
[88] E. Salehi, F.S. Azad, T. Harding, J. Abedi, Fuel Process. Technol. 92 (2011) 2203–2210.
[89] A. Oasmaa, I. Fonts, M.R. Pelaez-Samaniego, M.E. Garcia-Perez, M. Garcia-Perez, Energy Fuels 30 (2016) 6179–6200.